PUBLICATION

MUSTANG

A MUltiple Space and Time scale Approach for the quaNtification of deep saline formations for CO_2 storaGe

Project Number:227286

AUTHORS: *Victor Vilarrasa, Diogo Bolster, Sebastia Olivella, Jesus Carrera*

TITLE: *Coupled hydromechanical modeling of CO_2 sequestration in deep saline aquifers*

The research leading to these results has received funding from the European Community's Seventh Framework Programme [FP7/2007/2013) under grant agreement n° [227286]

Status	AUTHOR VERSION
Date	2013
Publisher	Elsevier
Reference	International Journal of Greenhouse Gas Control, Vol. 4, pp. 910–919

Submitted, accepted and published by Elsevier in *International Journal of Greenhouse Gas Control*, 4:910-919

DOI: 10.1016/j.ijggc.2010.06.006

COUPLED HYDROMECHANICAL MODELING OF CO_2 SEQUESTRATION IN DEEP SALINE AQUIFERS

VICTOR VILARRASA[1,2], DIOGO BOLSTER[1,3], SEBASTIA OLIVELLA[1], JESUS CARRERA[2]

[1]Department of Geotechnical Engineering and Geosciences, Civil Engineering School, Technical University of Catalonia, GHS, UPC, 08034 Barcelona, Spain.

[2]Institute of Environmental Assessment & Water Research, GHS, IDAEA, CSIC, 08028 Barcelona, Spain.

[3]Environmental Fluid Dynamics Laboratories, Dept of Civil Engineering, University of Notre Dame, IN 46556, USA

ABSTRACT

Sequestration of carbon dioxide (CO_2) in deep saline aquifers has emerged as an option for reducing greenhouse gas emissions to the atmosphere. The large amounts of supercritical CO_2 that need to be injected into deep saline aquifers may cause large fluid pressure increases. The resulting overpressure may promote reactivation of sealed fractures or the creation of new ones in the caprock seal. This could lead to escape routes for CO_2. In order to assess the probability of such an event, we model an axysimmetric horizontal aquifer-caprock system, including hydromechanical coupling. We study the failure mechanisms, using a viscoplastic approach. Simulations illustrate

that, depending on boundary conditions, the least favorable moment takes place at the beginning of injection. Initially, fluid pressure rises sharply because of a reduction in permeability due to desaturation. Once CO_2 fills the pores in the vicinity of the injection well and a capillary fringe is fully developed, the less viscous CO_2 displaces the brine and the capillary fringe laterally. The overpressure caused by the permeability reduction within the capillary fringe due to desaturation decreases with distance from the injection well. This results in a drop in fluid pressure buildup with time, which leads to a safer situation. Nevertheless, in the presence of low-permeability boundaries, fluid pressure continues to rise in the whole aquifer. This occurs when the radius of influence of the injection reaches the outer boundary. Thus, caprock integrity might be compromised in the long term.

1. INTRODUCTION

Carbon dioxide (CO_2) sequestration in deep saline aquifers is considered a promising mitigation option for the reduction of CO_2 emissions to the atmosphere. Injecting CO_2 into aquifers at depths greater than 800 m brings CO_2 to a supercritical state where its density is large enough to ensure an efficient use of pore space (Hitchon *et al*., 1999). Although the density of CO_2 can reach values as high as 900 kg/m^3, it will always be lighter than the resident brine. Consequently, it will flow along the top of the aquifer because of buoyancy. Thus, suitable aquifers should be capped by a low-permeability rock to avoid CO_2 migration to upper aquifers and the surface. Caprock discontinuities, such as fractured zones, may favor upwards CO_2 migration. Additionally, CO_2 injection can result in significant pressure buildup, which affects the stress field and may induce large deformations. These can eventually damage the caprock and open up new flow paths. These interactions between fluid flow and rock

mechanics are known as hydromechanical coupling.

Hydromechanical (HM) processes generally play an important role in geological media, and in particular during CO_2 injection into deep saline aquifers. These formations are usually fluid-saturated fractured rock masses. Therefore, they can deform either as a result of changes in external loads or internal pore pressures. This can be explained with direct and indirect HM coupling mechanisms (Rutqvist & Stephansson, 2003). Direct HM coupling consists of two phenomena: a solid-to-fluid coupling in which a variation in the applied load induces a change in porosity and thus in fluid pressure or mass; and a fluid-to-solid coupling that takes place when a change in fluid pressure or fluid mass causes a variation in the volume of the geological media. On the other hand, indirect HM coupling refers to changes in hydraulic or mechanical properties in response to strain.

In practice, using HM couplings allows us to determine conditions under which mechanical failure (shear failure or hydraulic fracture) could occur so that injection pressures can be limited below a fracturing threshold. Rutqvist *et al*. (2008) found that shear failure usually occurs at a lower injection pressure than hydro fracturing. When horizontal stress is greater than vertical stress ($\sigma_h > \sigma_v$), shear failure will occur preferentially in gently dipping fractures, without damage to the upper part of the caprock. However, when vertical stress is greater than horizontal stress ($\sigma_h < \sigma_v$) the propagation of fractures is most likely to occur in the form of steeply dipping fractures which could penetrate the entire caprock.

Existing simplified analytical solutions for determining the maximum sustainable pressure often predict incorrect values (Rutqvist *et al*., 2007, Vidal-Gilbert *et al*., 2008), suggesting that the fully coupled problem should be solved. Nonetheless, the majority of CO_2 injection simulations only model the multiphase flow problem (e.g.

Doughty & Pruess, 2004; Ide *et al*., 2007), without mechanical coupling. Some of these numerical studies reproduce pilot CO_2 injection tests (Doughty *et al*., 2006; Ghomian *et al*., 2008). Given that small quantities of CO_2 are usually injected in pilot tests, rock stability is not a concern. The computational burden is much higher using the hydromechanical coupling than the hydraulic problem (Tran *et al*., 2004). Nevertheless, coupling strategies are available to avoid the full coupling (i.e. solving the flow and mechanical problem together), such as explicit or iterative coupling or, even, decoupling. These schemes allow reducing the computational burden, but at the expense of some loss of accuracy (Mainguy & Longuemare, 2002; Settari & Walters, 1999).

The vast majority of rocks present very small yield stresses (Cristescu, 1989). As pressure buildup caused by CO_2 injection will affect a large extension of the aquifer and caprock over several decades, irreversible strains are expected to occur. However, poroelasticity is usually adopted to resolve the mechanical problem (Rutqvist *et al*., 2008, Vidal-Gilbert *et al*., 2008). Although this approach gives a good approximation, an elasto-plastic constitutive model provides more precise results (Settari & Walters, 1999).

Strains are induced by fluid pressure evolution, which depends on the hydraulic boundary conditions. Aquifers are sometimes assumed to be infinite (Rutqvist *et al*., 2008; van der Meer & van Wees, 2006). In modeling practice, this means that the boundary is placed far enough to ensure that it does not affect fluid flow. In fact, deep saline aquifers for CO_2 sequestration may extend tens or even hundreds of kilometers (McPherson & Cole, 2000; Zhang *et al*., 2009). However, CO_2 sequestration projects will span several decades. Therefore, the radius of influence ($R = \sqrt{2.25 k \rho_w g t / (\mu_w S_s)}$, where k is the intrinsic permeability, ρ_w is water density, g is gravity, t is time, μ_w is water viscosity and S_s is the specific storage coefficient of the aquifer) propagates over

large distances, reaching the boundaries much earlier than the end of operations (Birkholzer *et al*., 2009). In such cases, the infinite acting aquifer assumption may not be appropriate and the nature of the boundary may have to be addressed. Aquifers can be classified as open and semi-closed, depending on the nature of the boundaries. Open aquifers can be modeled with a constant head boundary condition (Lucier & Zoback, 2008), and semi-closed aquifers with a leakage coefficient. In open aquifers brine could escape and salinize fresh water bodies (Birkholzer & Zhou, 2009). In closed and semi-closed aquifers, the CO_2 storage capacity is basically controlled by rock and fluid compressibility (Vilarrasa *et al*., 2010; Zhou *et al*., 2008). Given that a low-permeability boundary can be modeled with a leakage coefficient, the role of such a boundary condition should be evaluated. The effect that a low-permeability boundary has on fluid flow has been studied in hydrogeology (e.g. Wheatcraft & Winterberg, 1985; Butler, 1988). Although these studies deal with single phase flows, they can be helpful and valid in two phase flows (e.g. Neuweiler *et al*., 2003; Bolster *et al*., 2009b). The other boundary condition that affects fluid pressure corresponds to that at the injection well. Various injection schemes have been studied using hydromechanical coupling, such as two-dimensional models that conceptually represent a large line of injection wells (e.g. Rutqvist & Tsang., 2002) and even a 3-D model simulating horizontal wells (Rutqvist *et al*., 2010). However, a single injection well with a radial flow, which can be represented by an axysimmetric model, has to our knowledge not yet been studied.

The aim of the present study is to investigate stress and strain during CO_2 injection in a single well using an axysimmetric model to assess caprock integrity. The relevance of plastic strains is examined along with the influence of the boundary conditions on fluid pressure evolution.

2. METHODS

2.1. Geometry

An ideal homogeneous horizontal aquifer-caprock system is considered for this study (Figure 1). The top of the 100 m thick aquifer is located at a depth of 1000 m. A 400 m thick low-permeability caprock overlies the aquifer and the caprock is covered by 600 m of media with low shear strength. These media do not need to be included in the model. The system is axysimmetric and extends laterally up to 1 km. An injection well with a radius of 0.15 m is placed at the centre of the domain.

2.2. Fluid Mechanics

The properties of the aquifer and caprock correspond to those of permeable sandstone (Dana & Skoczylas, 2002) and low-strength shale (Rutqvist *et al*., 2008), respectively (Table 1). Relative permeability follows a power law of saturation for both phases. In the aquifer it is a cubic law, while in the low-permeability caprock the power is 6. Retention curves follow the van Genuchten (1980) model (e.g. Rutqvist & Tsang, 2002; Zhou *et al*., 2008) (see Appendix A for the governing equations). We consider the aquifer to be a sandstone with homogeneous grain size. Therefore, the entry pressure is low and the shape parameter is high. These parameters favor CO_2 flow through the aquifer without a dramatic pressure buildup. On the other hand, caprock entry pressure is high, which hinders CO_2 migration.

The initial conditions are hydrostatic pressure and constant temperature of T=320 K. A constant head boundary condition is imposed on the outer boundary.

In order to determine the influence of the outer boundary condition on fluid pressure evolution, two purely hydraulic models were used. One that simulates an infinitely acting aquifer in which the lateral extent of the model is sufficient to ensure

that flow is independent of the nature of the boundary. The other consists of a low-permeability boundary placed 5 km from the injection well. The low-permeability boundary is imposed with a mixed or Cauchy boundary condition, which reads

$$Q = \alpha(P_0 - P) \tag{1}$$

where Q is the flow rate, α is the leakage coefficient, P_0 is the pressure of the external water body into which the aquifer leaks and P is fluid pressure. Three leakage coefficients, of 16, 32 and 64, are used to evaluate the effect of this low-permeability boundary. The lower the value of the leakage coefficient, the less permeable the outer boundary.

CO_2 is injected uniformly throughout the entire thickness of the aquifer at a constant rate of 79 kg/s (2.5 Mt/yr) and 113 kg/s (3.6 Mt/yr) for the purely hydraulic and the coupled hydromechanical simulations, respectively. The latter falls within the range of the CO_2 generated by a 400 MW coal-fired power plant.

As for the fluid properties, the formation brine, at the aquifer depths considered, has an initial density of 1087.5 kg/m^3 and a viscosity of $6 \cdot 10^{-4}$ Pa·s. Brine density depends on pressure, temperature and the amount of dissolved CO_2 in the brine. Brine viscosity depends only on temperature and is therefore constant for the isothermal case presented here. CO_2 density is calculated using the formulas of Span & Wagner (1996) and can vary significantly with pressure at the considered temperature T=320 K. The viscosity of CO_2 depends on temperature and CO_2 density (pressure). In this study, it is calculated with an expression proposed by Altunin & Sakhabetdinov (1972).

2.3. Geomechanics

The initial stress field displays a greater vertical than horizontal stress, $\sigma'_h = 0.65\sigma'_v$, where σ'_v is the lithostatic effective stress. The mechanical boundary

conditions are no displacement normal to the bottom and outer boundary. A constant, vertical lithostatic stress is imposed at the top of the caprock. We account for direct HM coupling, but we do not include strain dependent hydraulic properties.

The viscoplastic constitutive model adopted here is conceptually appropriate and computationally advantageous (Zienkiewicz & Cormeau, 1974; Zienkiewicz & Taylor, 2000). Most rocks present a very small yield stress. Furthermore, a significant pressure buildup will take place during CO_2 sequestration. Therefore, irreversible strains are expected to occur. This leads to the division of total strain into two parts

$$\mathrm{d}\boldsymbol{\varepsilon} = \mathrm{d}\boldsymbol{\varepsilon}^e + \mathrm{d}\boldsymbol{\varepsilon}^i \tag{2}$$

where $\boldsymbol{\varepsilon}^e$ is the elastic strain tensor and $\boldsymbol{\varepsilon}^i$ is the inelastic strain tensor.

The yield criterion is formulated in terms of invariants of the effective stress tensor

$$p' = \frac{1}{3}\left(\sigma'_x + \sigma'_y + \sigma'_z\right) = p - P_f \tag{3}$$

and

$$J_2 = \frac{1}{2}\mathrm{tr}\left(\mathbf{s}^{\mathrm{t}} : \mathbf{s}\right) = \frac{1}{3}q^2 \tag{4}$$

where p' is the mean effective stress, p is the mean stress, $P_f = \max\left(P_g, P_w\right)$ is fluid pressure, P_g is the gas pressure, P_w the water pressure and σ' denotes the effective stress. J_2 is the second invariant of $\mathbf{s} = \boldsymbol{\sigma}' - p'\mathbf{I}$ and then q is the equivalent deviatoric stress. The superscript t denotes transpose. The sign convention of soil mechanics is adopted, i.e. $p > 0$ represents compression.

The elastic strain increments can be decomposed into a volumetric strain and a deviatoric strain

$$\mathrm{d}\varepsilon_v^e = \frac{\mathrm{d}\,p'}{K}, \tag{5a}$$

$$\mathrm{d}\varepsilon_d^e = \frac{\mathrm{d}q}{3G} \tag{5b}$$

where ε_v^e and ε_d^e are the elastic volumetric strain and elastic deviatoric strain respectively, $K = E/(3(1-2\nu))$ is the bulk modulus, E is Young's modulus, ν is the Poisson ratio and $G = E/(2(1+\nu))$ is the shear modulus.

For the viscoplastic model, we adopted a Drucker-Prager yield function, F, defined as

$$F = q - Mp' - c\beta \tag{6}$$

where c is the cohesion and parameters M and β depend on the initial stress. For compression ($\sigma_1 > \sigma_2 = \sigma_3$)

$$M = \frac{6\sin\phi'}{3-\sin\phi'} \qquad \beta = \frac{6\cos\phi'}{3-\sin\phi'}, \tag{7}$$

and for extension ($\sigma_1 = \sigma_2 > \sigma_3$)

$$M = \frac{6\sin\phi'}{3+\sin\phi'} \qquad \beta = \frac{6\cos\phi'}{3+\sin\phi'}, \tag{8}$$

where ϕ' is the internal friction angle and c the cohesion, using the analogy with the Mohr-Coulomb yield criterion. $F < 0$ denotes elastic behaviour, and $F \geq 0$ implies viscoplastic strain, which are defined as

$$\frac{d\boldsymbol{\varepsilon}^i}{dt} = \Gamma\langle\Phi(F)\rangle\frac{\partial G}{\partial \boldsymbol{\sigma}'} \tag{9}$$

where t is time, Γ is a viscosity parameter, $\Phi(F)$ is a stress function, $\boldsymbol{\sigma}'$ is the effective stress tensor and G is the flow rule, which is given by

$$G = q - \alpha(Mp' + c\beta), \tag{10}$$

where α is a non-associativity parameter. The non-associativity parameter α can vary between 0 and 1. When α is zero, there is no dilatancy, and when α equals one, the model is associated and gives large dilatancy. In this study we consider α =0.3.

Finally, the stress function is defined as

$$\Phi(F) = F^m \tag{11}$$

where m is a constant power, which has been chosen as 3 for this study. It should be pointed out that both Γ and m are arbitrary in the sense that we are looking for an irreversible strain, which is not time dependent, and which essentially depends on the failure criteria. The analogy between viscoplasticity and plasticity is obtained from

$$d\boldsymbol{\varepsilon}^i = \Gamma\langle\Phi(F)\rangle dt \frac{\partial G}{\partial \boldsymbol{\sigma}'} = \Lambda \frac{\partial G}{\partial \boldsymbol{\sigma}'} \tag{12}$$

where Λ would be the plastic multiplier. So, for a sufficiently large Γ, the plasticity solution is recovered.

Mechanical failure can be assessed once the evolution of fluid pressure and related changes in the stress field are known. As stated in the introduction, two failure mechanisms can occur: hydraulic fracture and shear slip of pre-existing fractures. Hydraulic fracture occurs when fluid pressure exceeds the least compressive principal stress. This is a conservative assumption (Rutqvist *et al*., 2008) allowing for a safety factor. Thus, the critical pressure for hydrofracturing would be for a fracture with tension strength equal to zero

$$P_f \geq \sigma_3 . \tag{13}$$

As for the onset of shear slip, if a fracture of random orientation exists at any point, shear initiates plasticity when the deviatoric invariant q exceeds the yield function, i.e.

$$q \geq Mp' + c\beta . \tag{14}$$

The two conditions can also be put together for an existing fracture without cohesion using the following condition

$$F = q - Mp' \geq 0 . \quad (15)$$

2.4. Numerical solution

The injection of CO_2 into a homogeneous saline aquifer is simulated using the finite element numerical code CODE_BRIGHT (Olivella *et al*., 1994, 1996) modified for CO_2 injection. Quadrilateral elements are used to enable the calculation of the mechanical problem. The mesh, which is unstructured, consists of elements 10 m by 10 m located close to the injection well, both in the aquifer and the caprock. The size of element increases progressively away from the well up to a size of 30 m by 30 m at the outer boundary. As a first step, a steady-state calculation is carried out to ensure equilibrium for the pressure and stress fields.

3. FLUID PRESSURE EVOLUTION

3.1. Infinitely Acting Aquifer

Figure 2 displays the evolution of fluid pressure at the top of the injection well for an infinitely acting aquifer. The magnitude of the pressure buildup is inversely proportional to the permeability of the aquifer. Thus, the permeability of the aquifer may be a limiting factor. Injection pressure increases sharply when CO_2 injection starts. This sharp increase is maintained while a capillary fringe is being formed. This is because the relative permeability becomes very small when the porous media begins to desaturate. Once the capillary fringe is fully developed, pressure begins to drop (see Appendix B). At this stage, the pores in the vicinity of the well are filled with CO_2. Thus the fluid can flow more easily, because CO_2 viscosity is one order of magnitude

smaller than that of brine. The less viscous CO_2 displaces the brine and the capillary fringe laterally. The overpressure caused by the permeability reduction within the capillary fringe due to desaturation decreases with distance from the injection well (Figure 3). This results in a drop in fluid pressure buildup. This tendency is maintained until the CO_2-water interface is far enough so that the pressure drop due to the capillary fringe does not influence injection. This may occur for very long injection times (see Appendix B). Thereafter, fluid pressure starts increasing slightly.

3.2. Radial Aquifer with a Low-Permeability Boundary

The fluid pressure profile at the aquifer top for the case of a leakage coefficient equal to 16 is presented for several injection times in Figure 3. These profiles show the maximum pressure of either the CO_2 or the brine, i.e. the gas pressure in the CO_2 rich phase and the liquid pressure in the region occupied by the formation brine. A shoulder can be observed in all fluid pressure profiles. This increment corresponds to the edge of the CO_2 bubble and is due to both capillary pressure and the overall reduction in permeability within the capillary fringe. Fluid pressure at the injection well decreases after long injection times, as illustrated by comparing the curve after 1 year with that after 30 years of injection. However, note that fluid pressure increases in the entire aquifer. The pressure profile flattens and slowly increases its magnitude with time. Fluid pressure undergoes an increase of nearly 2 MPa at the low-permeability boundary during the first year of injection. It continues to increase for longer injection times, but at a very small rate.

Figure 4 displays the additional pressure increase for different values of the leakage coefficient, α, of the aquifer border. For a sufficiently high value of α, a constant head boundary condition is obtained. To maintain the flux for the imposed

Cauchy boundary condition at the outer boundary of the aquifer, the product between the leakage coefficient and the pressure gradient has to be constant (Equation (1)). For this reason, the lower the leakage coefficient, the greater the pressure gradient. Note that for the case where $\alpha = 16$ the pressure increase with respect to the constant head boundary condition is 1 MPa, which may be sufficient to induce mechanical failure. The overpressure in the presence of a permeable boundary with a constant head is lower because once the radius of influence reaches it, the growth of brine back pressure is stopped. From there on, injection pressure drops down because the displaced brine is more viscous than the invading CO_2. These are not necessarily good news, because it implies that a volume of brine equal to that of injected CO_2 is leaving the system, possibly to an adjacent freshwater body.

For a low-permeability boundary located at a distance greater than the one considered here, this fluid pressure increase behaviour would happen in the same manner, but delayed a time equal to $\mu_w S_s R^2 / (2.25 k \rho_w g)$, where R is the distance at which the low-permeability boundary is located. If the low-permeability boundary was located at a considerable distance from the injection well, the injection pressure would drop after the initial increase (Figure 2). However, once the radius of influence of the injection reached the low-permeability boundary, fluid pressure would increase in the whole aquifer (Figure 3). In particular, fluid pressure would also increase again at the injection well.

4. HYDROMECHANICAL COUPLING

CO_2 injection causes fluid pressure to increase, thus changing the effective stress tensor. The latter produces deformations of the medium, and these deformations exert an influence on the evolution of fluid pressure. Figure 5 compares a purely hydraulic

simulation (H) with a coupled hydromechanical (HM) simulation of the model presented in Figure 1. This coupled HM simulation uses the viscoplastic constitutive model outlined in Section 2.3. The difference between the purely hydraulic and the coupled hydromechanical simulations is small in the aquifer (Figure 5a). The two curves are almost parallel, with comparable asymptotic values of the pressures, and can be corrected by a translation, which depends on the storage coefficient selected. However, it is not easy to assign storativity values because the real relationship between stress and volumetric strain is very sensitive to strain mechanisms. Furthermore, HM simulation captures porosity changes due to rock strain (not only volumetric) in contrast to H simulation, which only considers a storage coefficient that includes fluid and rock compressibility (Mainguy & Longuemare, 2002). Thus, the two curves are not exactly parallel. Interestingly, the difference becomes significant in the caprock (Figure 5b). Hydraulic simulations do not capture the drop in the initial fluid pressure because of mechanical effects, such as dilatancy or bending of the caprock due to CO_2 injection. Thus, measuring fluid pressure in the caprock plays a major role in identifying the hydromechanical processes.

Figure 6 displays the evolution of stresses and pressures at the beginning of the injection. Fluid pressure in the aquifer and the caprock increases dramatically in response to the injection. Once the reservoir begins to desaturate, the gas and liquid pressure increase sharply, both in the reservoir and the caprock. As a result, the mean effective stress is reduced, which produces an expansion of the pore volume. Unlike the mean effective stress, the deviatoric stress is only slightly reduced, which compromises caprock integrity. This is the most critical period, as indicated by the maximum in the ratio between the deviatoric and the mean effective stresses. However, after the increase in the initial fluid pressure (and consequent decrease in the mean effective stress), the

liquid pressure will tend to stabilize. Thereafter, there is a decrease in gas and liquid pressure. As a result, the mean effective stress increases, but the deviatoric stress remains constant, and the ratio decreases. Therefore, for the conditions of our simulation, CO_2 injection becomes safer from the mechanical point of view as the injection time increases.

We consider the deviatoric stress q over a vertical section located in the vicinity of the injection well after 4 days of injection to study the risk of mechanical failure in the caprock (Figure 7) provided that parameters for a low-strength caprock are considered. The rock plastifies if the q exceeds the critical value, $q_{critic,}$ which is obtained from Equation (6) for F=0. Simulation results show that the rock plastifies at the contact point between the aquifer and the caprock. Similarly, the Mohr circle after 4 days of injection becomes tangent to the Mohr-Coulomb yield criterion (Figure 8). This implies that the caprock is damaged. The Mohr circle is displaced to the left over time, as expected because of increases in fluid pressure. Interestingly though, it shrinks, because horizontal stresses increase as horizontal strain is limited in the horizontal plane. Thus, lateral confinement ensures that the system becomes safer with time, i.e. if damage does not occur early it is unlikely to occur subsequently.

This behavior is also observed in the (q, p') plane for a point at the base of the caprock close to the well over an injection period of 100 days (Figure 9). Prior to injection (point A), the caprock is in the safe zone, at some distance from the plastic regime. Once injection begins, the mean effective stress decreases much more drastically than the deviatoric stress and the Mohr-Coulomb yield envelope is rapidly reached (point B). At this point, the rock begins to behave plastically. Thus, strain occurs plastically for a few days, until it reaches point C after 5 days of injection. Then, the deviatoric stress decreases at a higher rate than for the period between point B and

C, and the caprock ceases to plastify. Finally, the mean effective stress increases, reaching a safe situation again (point D) after 100 days of injection. In this particular case the rock plastifies, but there will be injection scenarios in which the (*q, p'*) trajectory will not reach the Mohr-Coulomb yield envelope. In these situations, the mobilized angle of friction of the caprock, i.e. the angle of friction that triggers plasticity can be determined. This mobilized angle of friction yields an estimate for the likelihood of mechanical failure in a given situation. This leads to the definition of a safety factor (*SF*) that is defined as follows

$$SF = \frac{\tan \phi'_{real}}{\tan \phi'_{mobilized}}, \tag{16}$$

where in this particular case of injection, the mobilized angle of friction is 17.2º. Whenever the actual angle of friction of the caprock is higher than this mobilized angle of friction, the injection safety factor is higher than one, indicating that it will be safe.

Figure 10 shows the plastic strain in the caprock in the vicinity of the injection well and the corresponding CO_2 bubble for different times close to the beginning of injection. Plastic strains evolve as CO_2 advances, but they stabilize after 5 days of injection. This is because a safe situation is reached, as shown by the (*q, p'*) trajectory in Figure 9. The plastic region propagates upwards and to the right with time as the CO_2 bubble increases in size, presenting a marked trend of maximum strain following a direction of approximately 45º to the ground surface. Once this plastic region stabilizes, it reaches horizontally a distance of 175 m from the injection well and 125 m above the base of the caprock. Note that the induced plastic strains are small (0.04 %), which suggests that the integrity of the caprock will not be compromised here.

Unlike horizontal displacements, vertical displacements can be significant (Vasco *et al*., 2008; Rutqvist *et al*., 2010). Figure 11 shows the vertical displacement that takes place at the top of the caprock, at a depth of 600 m, as a function of the

distance from the injection well at different injection times. The vertical displacement has a typical bell shape. The magnitude of the uplift gradually increases with time, reaching a maximum of several centimeters next to the injection well after 100 days of injection. This particular model does not simulate the upper 600 m of rock, but the vertical displacement should follow a similar trend, which means that a significant uplift of the ground could take place (Morris *et al.*, 2009).

5. DISCUSSION & CONCLUSIONS

We conducted simulations of CO_2 injection into a deep saline aquifer to study the risk of caprock mechanical failure. The specific scenario we model is meant to reflect a real world scenario. In particular, we assumed the material to be viscoplastic and the initial stress tensor to be axysimmetric with the vertical stress greater than the horizontal ones.

Given that instability is caused by fluid pressure buildup, we carried out hydraulic simulations of an infinitely acting aquifer and a circular aquifer with a low-permeability boundary to study the influence of the boundary condition. Exclusion of the mechanical component allowed us to run the simulations at a reasonably low computational cost. We found that after an initial sharp increase, the fluid pressure drops. This occurs because the less viscous CO_2 displaces brine and the capillary fringe laterally. This capillary fringe produces an overpressure because of permeability reduction due to desaturation. This overpressure decreases with distance from the injection well. Thus, fluid pressure decreases with time. This drop in fluid pressure may allow the injection of an additional amount of CO_2 without compromising the caprock stability. Furthermore, the measurement of this fluid pressure drop in field tests (with constant injection mass rate) can give valuable information about the capillary fringe.

If the aquifer has a low-permeability boundary, fluid pressure can rise again once the radius of influence reaches this boundary. This increase takes place in the whole aquifer. This additional overpressure may induce rock failure in the long term. In most CO_2 sequestration projects, the boundaries of the basins will play a role in the injection since CO_2 sequestration projects are planned to take place over long periods of time (several decades). Over such timescales the radius of influence will reach tens and even hundreds of kilometers, depending on the permeability of the aquifer. Thus, the geometry and hydraulic properties of the aquifer boundaries should be characterized in detail.

Full coupling in hydromechanical simulations leads to lower increases in fluid pressure than the use of purely hydraulic simulations. This occurs because of rock deformations. The difference can be small in the aquifer if a good estimate of the storage coefficient is used. However, the evolution of fluid pressure is completely different in the caprock because of mechanical effects such as dilatancy and bending of the caprock due to CO_2 injection. In these coupled simulations we consider direct HM couplings, but not indirect HM ones (such as changes in permeability due to porosity changes (Rutqvist & Tsang, 2002)). The incorporation of indirect HM couplings might lead to significant differences in the results. On the other hand, direct HM couplings consider rock strain and changes in the stress field (Figure 8). CO_2 injection increases fluid pressure and as a result the rock deforms leading to changes in the porosity. This deformation increases the pore volume, resulting in a drop in fluid pressure. Despite this drop in fluid pressure, a sufficiently large overpressure occurs in the reservoir, inducing plastic strain in the caprock at the beginning of the injection. In this work, the caprock mechanical strength was intentionally chosen so that the rock plastifies as our goal was to determine failure mechanisms that could serve as an escape route for CO_2.

In practice, it is essential to determine the *in situ* stress field. The failure mechanisms discussed here could be expected for cases where the vertical stress is greater then the horizontal stresses. From a mechanical perspective, the analysis of the (*q, p'*) trajectories illustrates that the most critical period occurs in the early stages for a constant injection rate. The stress state can be close to failure during this period. Failure will occur when the yield surface is reached, giving rise to plastic strain, which may result in microfracturing (i.e. detectable by a local seismic network). Yield is local, so that the break up of caprock is unlikely. Nonetheless, monitoring caprock integrity at the beginning of the injection is crucial to ensure a safe injection. As shown in Figure 10, the caprock could yield at the beginning of the injection and the damage could propagate through a portion of the caprock. Furthermore, if a weak zone was already present in the caprock, the damage would be greater and preferential paths could be created, allowing the CO_2 to migrate up to shallow aquifers or even the ground surface. If the CO_2 can penetrate into the caprock, geochemical interactions will take place due to its acidity.

To limit local failure at the beginning of injection, a good characterization of the caprock is necessary. If the strength of the rock was known, numerical simulations would enable us to determine a sustainable injection pressure. This may be achieved by determining the mobilized angle of friction and by ensuring that it does not exceed the real friction angle of the rock even in weak zones. The use of a safety factor (Equation (16)) can be valuable in probabilistic risk assessment (e.g. Tartakovsky, 2007; Bolster *et al*., 2009a).

In this study, a homogeneous caprock is considered. Heterogeneities in the caprock, such as weak zones, fractured zones or discontinuities, are likely to be present in most injection areas. Furthermore, given that CO_2 injection projects are planned to

last decades, the CO_2 bubble will span several kilometers. Therefore, future studies should address the influence of mechanical and hydraulic heterogeneities in the caprock in order to simulate more realistic situations.

We modified and used the program CODE_BRIGHT to study the coupled hydromechanical evolution in an aquifer-caprock system during CO_2 sequestration in deep saline aquifers. In summary, the main conclusions drawn from this study are:

- Fluid pressure begins to drop once the capillary fringe is fully developed. The overpressure produced within the capillary fringe (because of permeability reduction due to desaturation) decreases with the distance from the well. Measuring this fluid pressure drop in field tests can give valuable information about the capillary fringe. Furthermore, an additional amount of CO_2 may be injected with a small increase in fluid pressure.
- If the aquifer has a low-permeability boundary, fluid pressure can rise once the radius of influence reaches the outer boundary. As a result of this, the mechanical integrity of the caprock could be compromised in the long term.
- The lower zone of the caprock presents the largest hydromechanical changes, presenting the greatest risk of rock failure, particularly in the early stages of injection.
- Slowly increasing the injection rate at the beginning of injection is recommendable in order to reduce possible damage to the caprock. Furthermore, measuring fluid pressure in the caprock is essential for identifying hydromechanical processes.
- Numerical simulations allow us to estimate the maximum sustainable injection pressure given the strength of the caprock. A safety factor can be defined by determining the mobilized angle of friction.

ACKNOWLEDGEMENTS

V.V. and D.B. would like to acknowledge the Spanish Ministry of Science and Innovation (MIC) for financial support through the "Formación de Profesorado Universitario" and "Juan de la Cierva" programs. V.V. also wishes to acknowledge the "Colegio de Ingenieros de Caminos, Canales y Puertos – Catalunya" for their financial support. This project has been funded by the Spanish Ministry of Science and Innovation through the CIUDEN project (Ref.: 030102080014), and through the MUSTANG project, from the European Community's Seventh Framework Programme FP7/2007-2013 under grant agreement nº 227286.

APPENDIX A. Coupled HM formulation for CO_2 flow

The balance equations required for the solution of the problems studied in this paper are presented in this appendix. Olivella et al. (1994) have presented the governing equations for non-isothermal multiphase flow of water and gas through porous deformable media. A detailed derivation is given there, and only a description of the modified formulation for gas (CO_2) flow is presented in this appendix.

The mass balance of solid present in the medium is written as

$$\frac{\partial}{\partial t}\left(\rho_s\left(1-\phi\right)\right)+\nabla\cdot\left(\mathbf{j}_s\right)=0 \tag{A1}$$

where ρ_s is the density of solid and $\mathbf{j}_s$ is the flux of solid. From this equation, an expression for porosity variation can be obtained if the flux of solid is written as the velocity of the solid multiplied by the volumetric fraction occupied by the solid phase and its density, i.e. $\mathbf{j}_s=\rho_s\left(1-\phi\right)\frac{d\mathbf{u}}{dt}$,

$$\frac{D_s\phi}{Dt} = \frac{(1-\phi)}{\rho_s}\frac{D_s\rho_s}{Dt} + (1-\phi)\nabla\cdot\frac{d\mathbf{u}}{dt} \tag{A2}$$

The material derivative with respect to the solid is defined as

$$\frac{D_s(\bullet)}{Dt} = \frac{\partial(\bullet)}{\partial t} + \frac{d\mathbf{u}}{dt}\cdot\nabla(\bullet) \tag{A3}$$

Equation (A2) expresses the variation of porosity caused by volumetric deformation and solid density variation.

In the formulation required for the analysis in this paper, gas and liquid phases are considered. The total mass balance of a component *i* present in each phase (for instance dissolved CO_2 or evaporated water) is expressed as

$$\frac{\partial}{\partial t}\left(\omega_l^i\rho_l S_l\phi + \omega_g^i\rho_g S_g\phi\right) + \nabla\cdot\left(\mathbf{j}_l^i + \mathbf{j}_g^i\right) = f^i \tag{A4}$$

where S_l, S_g are the phase degree of saturations; ω_l^i, ω_g^i are the mass fractions of the component *i* in each phase; ρ_l, ρ_g are the phase densities, $\mathbf{j}_l^i, \mathbf{j}_g^i$ are the mass fluxes of the component *i* in each phase and f^i is an external supply of mass of component *i*. In this formulation the components are the water and CO_2. The mass flux of components is a combination of a non-advective flux (diffusion + dispersion) written as $\mathbf{i}_l^i, \mathbf{i}_g^i$, the advective Darcy flux written as $\mathbf{q}_l, \mathbf{q}_g$ and another advective term caused by the solid motion proportional to the solid velocity $d\mathbf{u}/dt$:

$$\frac{\partial}{\partial t}\left(\omega_l^i\rho_l S_l\phi + \omega_g^i\rho_g S_g\phi\right) + \nabla\cdot\left(\mathbf{i}_l^i + \mathbf{i}_g^i + \omega_l^i\rho_l\mathbf{q}_l + \omega_g^i\rho_g\mathbf{q}_g + \left(\omega_l^i\rho_l S_l + \omega_g^i\rho_g S_g\right)\phi\frac{d\mathbf{u}}{dt}\right) = f^i \tag{A5}$$

The use of the material derivative leads to

$$\begin{aligned}&\phi\frac{D_s\left(\omega_l^i\rho_l S_l + \omega_g^i\rho_g S_g\right)}{Dt} + \left(\omega_l^i\rho_l S_l + \omega_g^i\rho_g S_g\right)\frac{D_s\phi}{Dt} + \left(\omega_l^i\rho_l S_l + \omega_g^i\rho_g S_g\right)\phi\nabla\cdot\left(\frac{d\mathbf{u}}{dt}\right) + \\ &+\nabla\cdot\left(\mathbf{i}_l^i + \mathbf{i}_g^i + \omega_l^i\rho_l\mathbf{q}_l + \omega_g^i\rho_g\mathbf{q}_g\right) = f^i\end{aligned} \tag{A6}$$

The mass balance of solid is introduced in the mass balance of a component to obtain, after some algebra,

$$\phi \frac{D_s\left(\omega_l^i \rho_l S_l + \omega_g^i \rho_g S_g\right)}{Dt} + \left(\omega_l^i \rho_l S_l + \omega_g^i \rho_g S_g\right)\frac{(1-\phi)}{\rho_s}\frac{D_s \rho_s}{Dt} + \\ + \left(\omega_l^i \rho_l S_l + \omega_g^i \rho_g S_g\right)\nabla \cdot \left(\frac{d\mathbf{u}}{dt}\right) + \nabla \cdot \left(\mathbf{i}_l^i + \mathbf{i}_g^i + \omega_l^i \rho_l \mathbf{q}_l + \omega_g^i \rho_g \mathbf{q}_g\right) = f^i \quad \text{(A7)}$$

The volumetric deformation term ($d\varepsilon_v/dt = \nabla \cdot (d\mathbf{u}/dt)$) couples the mass balance equations with the deformations of the medium. This requires the coupled solution of the mechanical equations. If the inertial terms are neglected, the momentum balance for the porous medium reduces to the equilibrium of stresses

$$\nabla \cdot \boldsymbol{\sigma} + \mathbf{b} = \mathbf{0} \quad \text{(A8)}$$

where $\boldsymbol{\sigma}$ is the stress tensor and **b** is the vector of body forces.

The simultaneous solution of the coupled equations given above produces the spatial and temporal evolution of displacements, liquid pressure and CO_2 pressure. These are considered as state variables or unknowns in this approach.

APPENDIX B. Pressure evolution with time

Fluid pressure buildup can be divided into three parts. One corresponding to fluid pressure buildup in the brine phase (ΔP_1), another in the CO_2 phase (ΔP_3) and a third corresponding to a capillary fringe which is partially saturated with CO_2 (ΔP_2) (Fig. 3). This capillary fringe defines the interface between CO_2 and brine. Assuming, for the purpose of pressure buildup calculations, that the interface is (sub)vertical, the pressure buildup for brine and CO_2 phases can be calculated using Thiem's solution (Thiem, 1906). Pressure loss across the capillary fringe is approximated by means of a leakage coefficient

$$\Delta P_1 = \frac{Q\mu_w}{2\pi kb} \ln \frac{R}{R_i}, \tag{B1}$$

$$\Delta P_2 = \frac{Q}{2\pi R_i \gamma}, \tag{B2}$$

$$\Delta P_3 = \frac{Q\mu_c}{2\pi kb} \ln \frac{R_i}{r_w}, \tag{B3}$$

where Q is the volumetric CO_2 flow rate, μ_w and μ_c are the viscosity of brine and CO_2, respectively, k is the intrinsic permeability of the aquifer, b is the aquifer thickness, R is the radius of influence, R_i is the radius of the interface between CO_2 and brine, r_w is the well radius and γ is a leakage coefficient. This leakage coefficient characterizes the pressure drop across the capillary fringe that can be observed in Figure 3. As the relative permeability to both CO_2 and aqueous phases drops significantly with saturation, displacement of the capillary fringe requires some extra energy. The leakage coefficient can be seen as the conductance of the capillary fringe. Consequently, it is derived from the harmonic average of effective permeability across the capillary fringe. Therefore it will be quite sensitive to the adopted relative permeability functions and to the thickness of the capillary fringe. Here, we assume γ approximately constant, which appears consistent with the reduction of ΔP_2 away from the injection well. However, the leakage coefficient probably decreases with distance from the well (see Fig. 3).

The radius of influence is given by

$$R = \sqrt{\frac{2.25 k_w \rho_w g t}{\mu_w S_s}} \tag{B4}$$

where ρ_w is the brine density, g is gravity, t is time and S_s is the specific storage coefficient. The radius of the interface between CO_2 and brine can be approximated as

$$R_i = \sqrt{\frac{Qt}{\pi b \theta_c}}\,, \tag{B5}$$

where θ_c is the volumetric content of CO_2. Note that both radii grow with the square root of time. Thus, ΔP_1 is time independent.

To analyze the time evolution of ΔP, we derive pressure buildup with respect to time

$$\frac{d}{dt}\left(\Delta P_1 + \Delta P_2 + \Delta P_3\right) = 0 + \frac{Q}{2\pi}\left(-\frac{1}{R_i^2 \gamma} + \frac{\mu_c}{k_c b R_i}\right)\frac{dR_i}{dt}\,. \tag{B6}$$

For small R_i the derivative is negative because the first term (negative) is inversely proportional to R_i^2 and will be greater than the other term (positive), which is inversely proportional to R_i. The fluid pressure buildup will increase when the capillary fringe is at such a distance that the pressure drop due to capillary forces does not affect the injection. The condition for this to occur is

$$R_i > \frac{k_c b}{\mu_c \gamma}, \tag{B7}$$

which may be quite large. In our simulations, pressure started to increase after some 10 years of injection, for which R_i equals 2200 m.

REFERENCES

Altunin, V. V. & Sakhabetdinov, M. A., 1972. Viscosity of liquid and gaseous carbon dioxide at temperatures 220-1300 K and pressure up to 120 bar. *Teploenergetika, 8*, 85–89.

Birkholzer, J. T., Zhou, Q. & Tsang, C.-F., 2009. Large-scale impact of CO_2 storage in deep saline aquifers: A sensitivity study on pressure response in stratified systems. *International Journal of Greenhouse Gas Control, 3*, 181–194.

Birkholzer, J. T. & Zhou, Q., 2009. Basin-scale hydrogeologic impacts of CO_2 storage: Capacity and regulatory implications. *International Journal of Greenhouse Gas Control, 3*, 745–756.

Bolster, D., Barahona, M., Dentz, M., Fernandez-Garcia, D., Sanchez-Vila, X., Trinchero, P., Valhondo, C. & Tartakovsky, D.M., 2009a. Probabilistic risk analysis of groundwater remediation strategies. *Water Resources Research, 45 W06413*, doi: 10.1029/2008WR007551.

Bolster, D., Dentz, M. & Carrera, J., 2009b. Effective two phase flow in heterogeneous media under temporal pressure fluctuations. *Water Resources Research*, *45:W05,408,* doi: 1029/2008WR007, 460.

Butler, J. J. J., 1988. Pumping test in nonuniform aquifers – the radially symmetric case. *Journal of Hydrology, 101*, 15–30.

Cristescu, N. (ed), 1989. Rock Rheology. Kluwer Academic Publishers. Dordrecht.

Dana, E. & Skoczylas, F., 2002. Experimental study of two-phase flow in three sandstones. II. Capillary pressure curve measurement and relative permeability pore space capillarity models. *International Journal of Multiphase Flow, 28*, 1965–1981.

Doughty, C. & Pruess K. (2004). Modeling Supercritical Carbon Dioxide Injection in Heterogeneous Media. *Vadose Zone Journal, 3*, 837–847.

Doughty, C., Freifeld, B.M. & Trautz, R.C. (2006). Site characterization for CO2 geologic storage and vice versa: the Frio brine pilot, Texas, USA as a case study. *Environmental Geology, 54*, 1635–1656.

Ghomian, Y., Pope, G.A. & Sepehrnoori, K. (2008). Reservoir simulation of CO_2 sequestration pilot in Frio brine formation, USA Gulf Coast. *Energy, 33*, 1055–1067.

Hitchon, B., Gunter, W. D., Gentzis, T. & Bailey, R. T., 1999. Sedimentary basins and greenhouse gases: a serendipitous association. *Energy Conversion & Management, 40*, 825–843.

Ide, S. T., Jessen, K. & Orr Jr, F. M., 2007. Storage of CO_2 in saline aquifers: Effects of gravity, viscous, and capillary forces on amount and timing of trapping. *International Journal of Greenhouse Gas Control, 1*, 481–491.

Lucier, A. & Zoback, M., 2008. Assessing the economic feasibility of regional deep saline aquifer CO_2 injection and storage: A geomechanics-based workflow applied to the Rose Run sandstone in Eastern Ohio, USA. *International Journal of Greenhouse Gas Control, 1*, 230–247.

Mainguy, M. & Longuemare, P., 2002. Coupling fluid flow and rock mechanics: formulations of the partial coupling between reservoir and geomechanical simulators. *Oil & Gas Science and Technology, 57 (4)*, 355–367.

McPherson, B. J. O. L. & Cole, B. S., 2000. Multiphase CO_2 flow, transport and sequestration in the Powder River Basin, Wyoming, USA. *Journal of Geochemical Exploration, 69-70*, 65–69.

Morris, J P ; McNab, W W ; Carroll, S K ; Hao, Y ; Foxall, W ; Wagoner, J L, 2009. ”Injection and Reservoir Hazard Management: The Role of Injection-Induced Mechanical Deformation and Geochemical Alteration at In Salah CO2 Storage Project: Status Report Quarter end, June 2009" LLNL Technical Report, DOI 10.2172/964517

Neuweiller, I., Attinger, S., Kinzelbach, W. & King, P., 2003. Large scale mixing for immiscible displacement in heterogeneous porous media. *Transp Porous Media, 51*, 287–314.

Olivella, S., Carrera, J., Gens, A. & Alonso E. E., 1994. Non-isothermal multiphase flow of brine and gas through saline media. *Transp Porous Media, 15*, 271–293.

Olivella, S., Gens, A., Carrera, J. & Alonso E. E., 1996. Numerical formulation for a simulator (CODE_BRIGHT) for the coupled analysis of saline media. *Eng Computations, 13*, 87–112.

Rutqvist, J., Birkholzer, J. T., Cappa, F. & Tsang, C-F., 2007. Estimating maximum sustainable injection pressure during geological sequestration of CO_2 using coupled fluid flow and geomechanical fault-slip analysis. *Energy Conversion & Management, 48*, 1798–1807.

Rutqvist, J., Birkholzer, J. T. & Tsang, C-F., 2008. Coupled reservoir–geomechanical analysis of the potential for tensile and shear failure associated with CO_2 injection in multilayered reservoir–caprock systems. *Rock Mechanics and Mining Sciences, 45*, 132–143.

Rutqvist, J. & Stephansson, O., 2003. The role of hydromechanical coupling in fractures rock engineering. *Hydrogeology Journal, 11*, 7–40.

Rutqvist, J. & Tsang, C-F., 2002. A study of caprock hydromechanical changes with CO_2 injection into a brine formation. *Environmental Geology, 42*, 296–305.

Rutqvist, J., Vasco, D.W. & Myer, L., 2010. Coupled reservoir-geomechanical analysis of CO_2 injection and ground deformations at In Salah, Algeria. *International Journal of Greenhouse Gas Control, 4 (2),* 225–230.

Settari, A. & Walters, D. A., 1999. Advances in coupled geomechanical and reservoir modeling with applications to reservoir compaction. *SPE Reservoir Simulator Symposium,* 14-17 Feb, Houston, Texas.

Span, R. & Wagner, W., 1996. A new equation of state for carbon dioxide covering the fluid region from the triple-point temperature to 1100 K at pressures up to 88 MPa. *J. Phys. Chem. Ref. Data, 25 (6)*, 1509–1595.

Tartakovsky, D.M., 2007. Probabilistic risk analysis in subsurface hydrology. *Geophys Res Lett 34, L05, 404.*

Thiem, G. (ed), 1906. Hydrologische Methode. Leipzig, Gebhardt.

Tran, D., Settari, A. & Nghiem, L., 2004. New iterative coupling between a reservoir simulator and a geomechanics module. *Society of Petroleum Engineers Journal, SPE/ISRM Rock Mechanics Conference,*20-23 Oct, Irving, Texas, USA, 362–369.

van der Meer, L. H. G. & van Wees, J. D., 2006. Limitations to storage pressure in finite saline aquifers and the effect of CO_2 solubility on storage pressure. *SPE Annual Technical Conference and Exhibition*, 24-27 Sep, San Antonio, Texas, USA.

van Genuchten, R., 1980. A closed-form equation for predicting the hydraulic conductivity of unsaturated soils. *Soil Sci. Soc. Am. J., 44*, 892 – 898.

Vasco, D.W., Ferretti, A. & Novali, F., 2008. Reservoir monitoring and characterization using satellite geodetic data: Interferometric Synthetic Aperture Radar observations from the Krechba field, Algeria. *Geophysics 73 (6),* WA113–WA122.

Vidal-Gilbert, S., Nauroy, J-F. & Brosse, E., 2009. 3D geomechanical modelling for CO_2 geologic storage in the Dogger carbonates of the Paris Basin. *International Journal of Greenhouse Gas Control, 3*, 288–299.

Vilarrasa, V., Bolster, D., Dentz, M., Olivella, S. & Carrera, J., 2009. Effects of CO_2 compressibility on CO_2 storage in deep saline aquifers. *Transport In Porous Media,* DOI: 10.1007/s11242-010-9582-z.

Wheatcraft, S. W. & Winterberg, F., 1985. Steady state flow passing through a cylinder of permeability different from the surrounding medium. *Water Resources Research, 21 (12)*, 1923–1929.

Zhang, W., Li, Y., Xu., T., Cheng, H., Zheng, Y. & Peng, X., 2009. Long-term variations of CO_2 trapped in different mechanisms in deep saline formations: A case study of the Songliao Basin, China. *International Journal of Greenhouse Gas Control, 3*, 161–180.

Zhou, Q., Birkholzer, J., Tsang, C-F. & Rutqvist, J., 2008. A method for quick assessment of CO_2 storage capacity in closed and semi-closed saline formations. *International Journal of Greenhouse Gas Control, 2*, 626–639.

Zienkiewicz, O. C. & Cormeau, I. C., 1974. Viscoplasticity, plasticity and creep in elastic solids: a unified numerical solution approach. *Int. J. Numer. Methods Engng 8*, 821–845.

Zienkiewicz, O. C. & Taylor, R. L., 2000. The finite element method. Vol 2: Solid mechanics. Oxford: Butterworth-Heinemann.

Table 1.- Material properties used in the hydromechanical analysis of the aquifer –

caprock system

Property	***Aquifer***	***Caprock***
Young's modulus, E (MPa)	$1{\cdot}10^{4}$	$5{\cdot}10^{3}$
Poisson's ratio, v (–)	0.3	0.3
Porosity, $\emptyset$ (–)	0.1	0.01
Cohesion, c' (MPa)	0.01	0.01
Parameter M (–)	1.2	0.65 *
Parameter β (–)	2.08	2.12
Permeability, k (m^2)	$1{\cdot}10^{-13}$	$1{\cdot}10^{-16}$
Relative liquid permeability, k_{rl} (–)	S_l^3	S_l^6
Relative gas permeability, k_{rg} (–)	S_g^3	S_g^6
Gas entry pressure, P_0 (MPa)	0.02	0.6
Van Genuchten m (–)	0.8	0.5

*: Low value taken to obtain irreversible strain

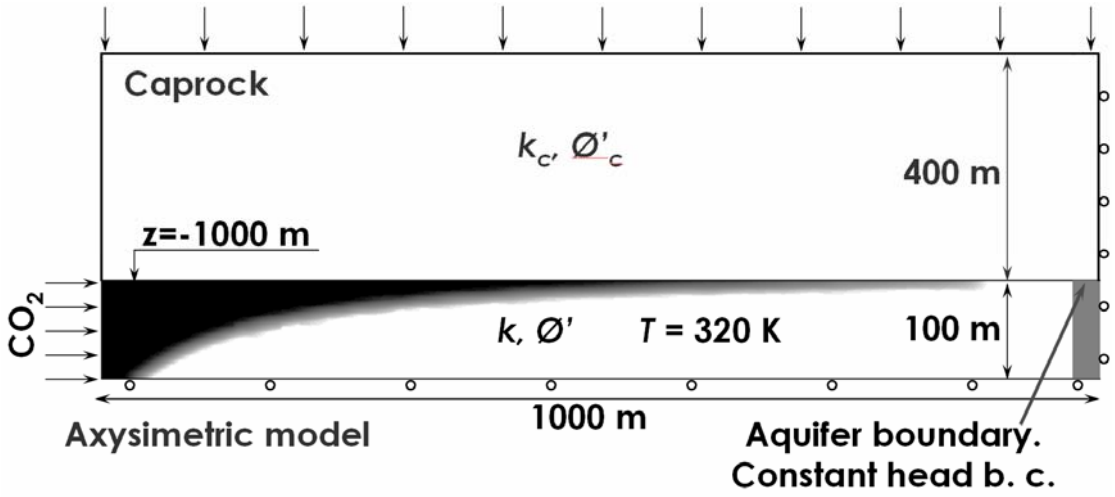

Figure 1: Schematic of description model geometry and boundary conditions.

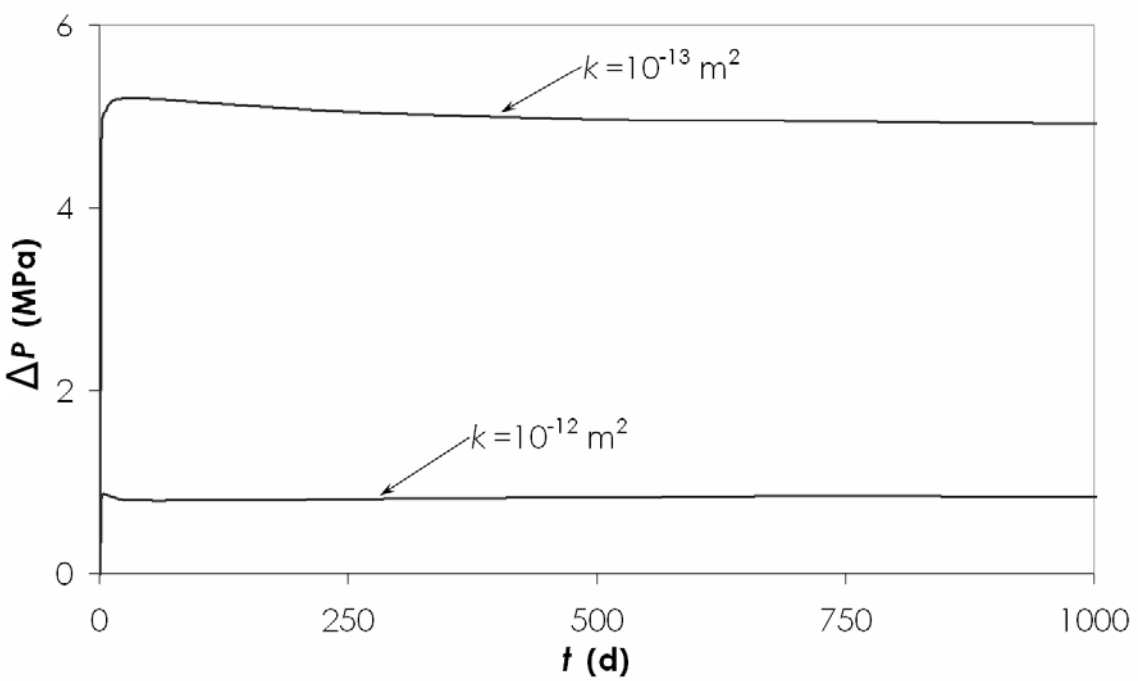

Figure 2: Injection pressure at the top of the aquifer for a 1000 day injection period, for two intrinsic permeabilities of the aquifer. Injection pressure drops because of the lower CO_2 viscosity with respect to that of brine.

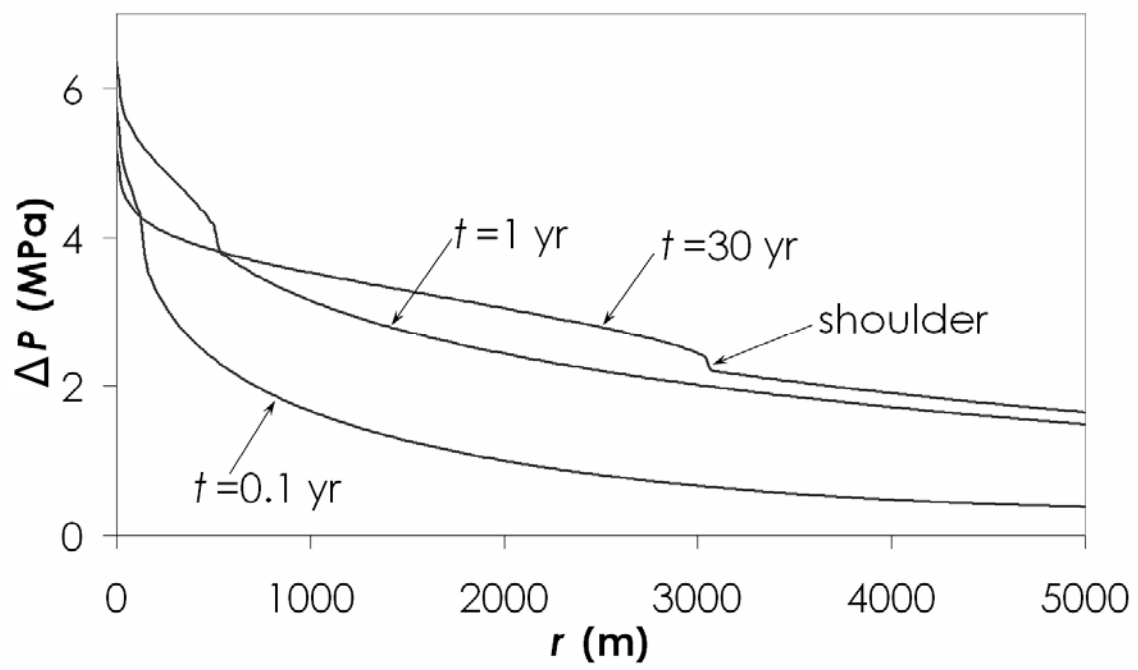

Figure 3: Fluid overpressure at the top of the aquifer as a function of the distance from the injection well for different injection times when the aquifer presents a low-permeability boundary at 5 km from the injection well. Note the shoulder in pressure observed near the CO_2-water interface. The pressure drop across this interface decreases with distance from the well because the overall permeability drops in response to partial desaturation.

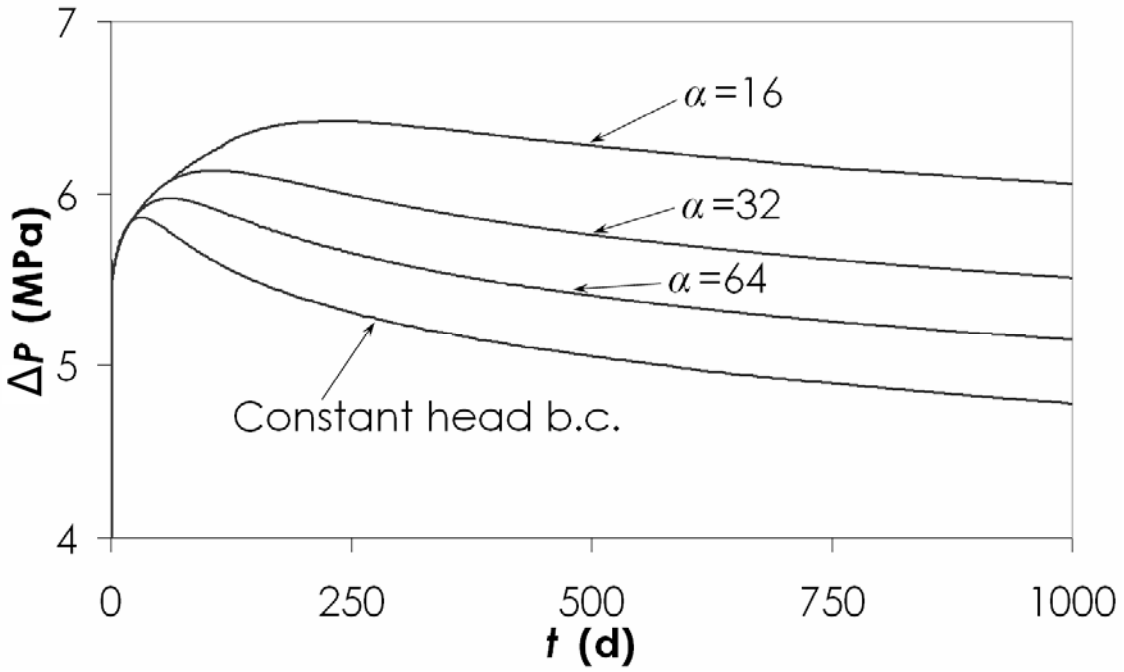

Figure 4: Overpressure at the injection well at the top of the aquifer for a 1000 day injection period for different leakage coefficients of the aquifer boundary placed 5 km away from the injection well.

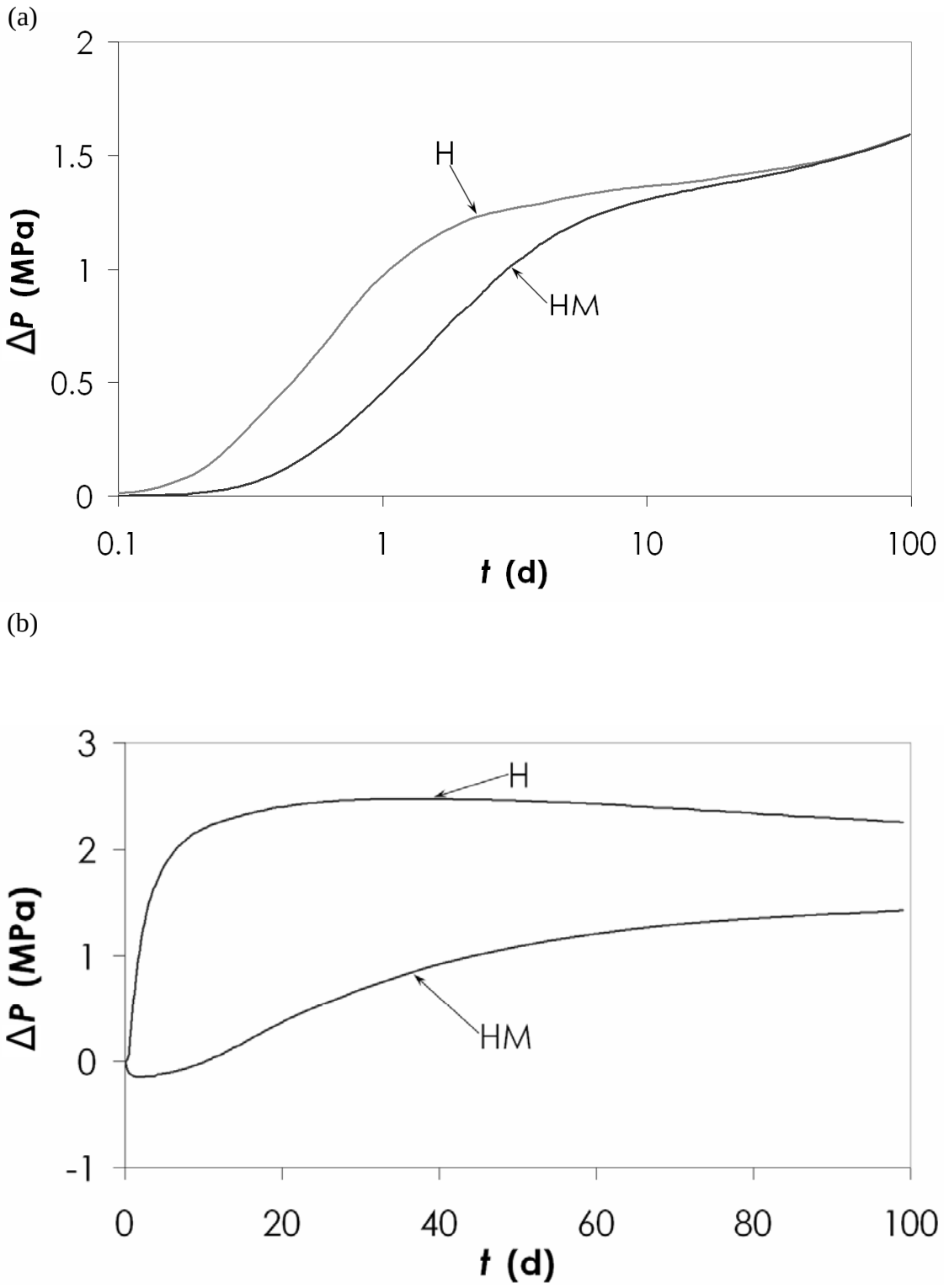

Figure 5: Fluid overpressure for a 100 days injection period, comparing pure hydraulic (H) with coupled hydromechanical (HM) simulation in (a) the aquifer at the contact between the aquifer and the caprock 400 m from the injection well and (b) in the caprock 50 m above the aquifer and 50 m away the injection well.

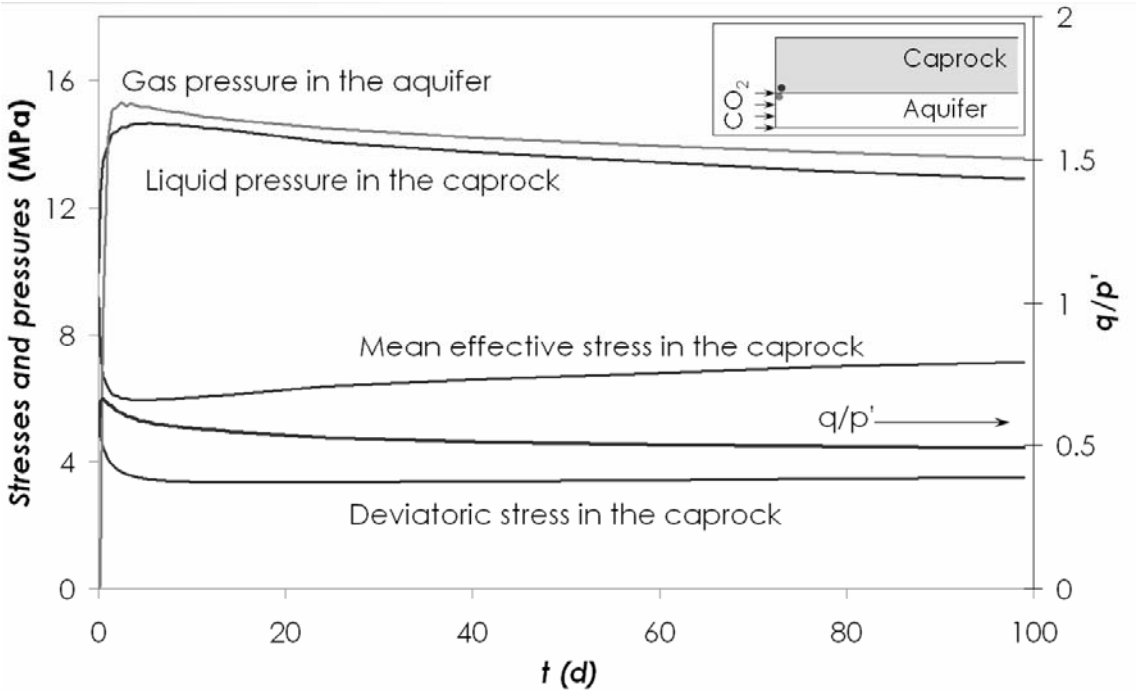

Figure 6: Stress and pressure evolution with time at the beginning of CO_2 injection at the base of the caprock next to the injection well (see location in inset).

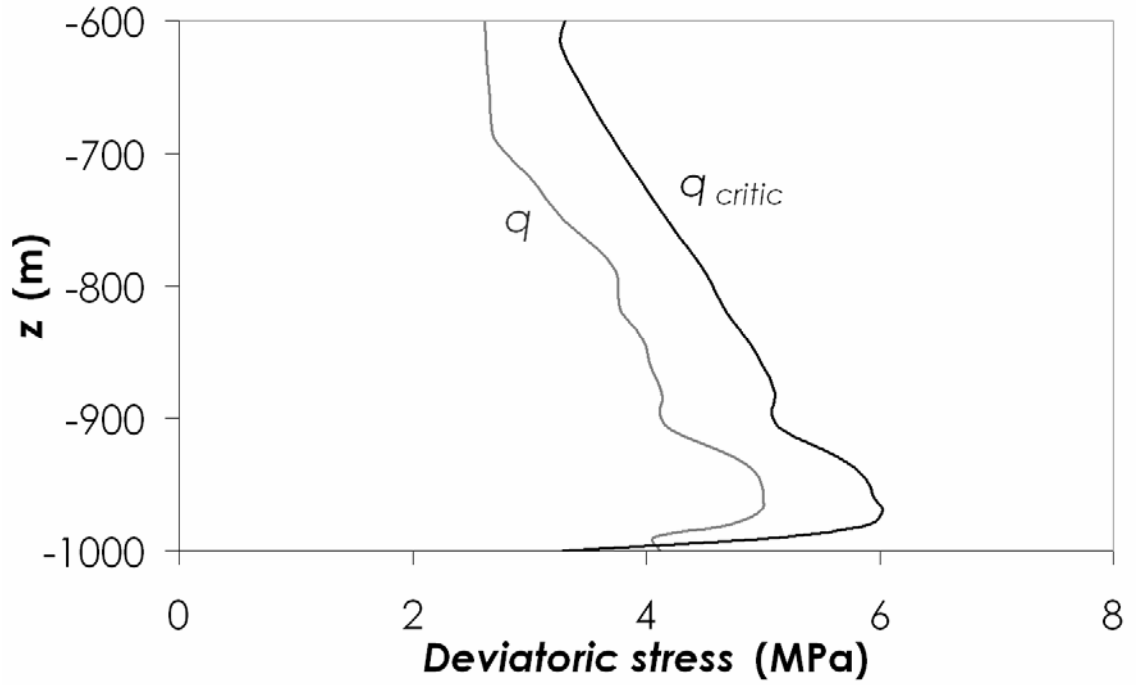

Figure 7: A vertical section of the caprock in the vicinity of the well, with the deviatoric stress, q, and critical the deviatoric stress, q_{critic}, after 4 days of injection. Note that q exceeds q_{critic} in the contact between the caprock and the aquifer, thus causing the caprock to plastify.

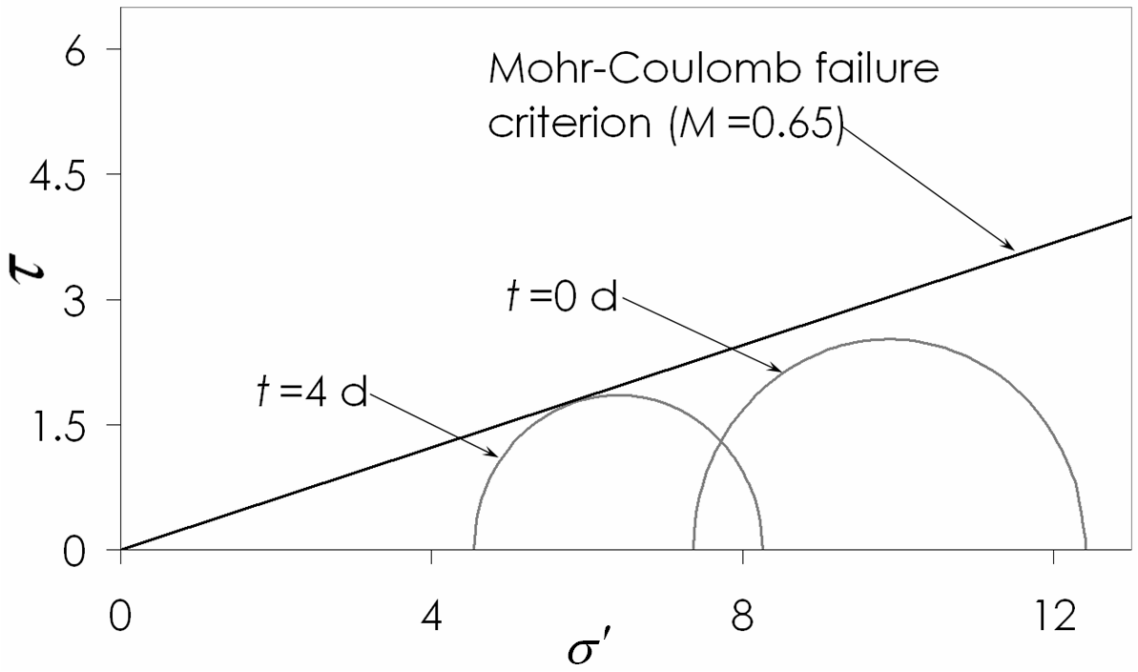

Figure 8: Mohr circles at the initial state and after 4 days of injection. The parameters of the Mohr-Coulomb failure criterion are $c = 0$ and $\phi' = 17.2^{o}$ (low value taken to obtain irreversible strain). The Mohr circle after 4 days of injection is displaced to the left (reduction in p') and is reduced in size (reduction in q).

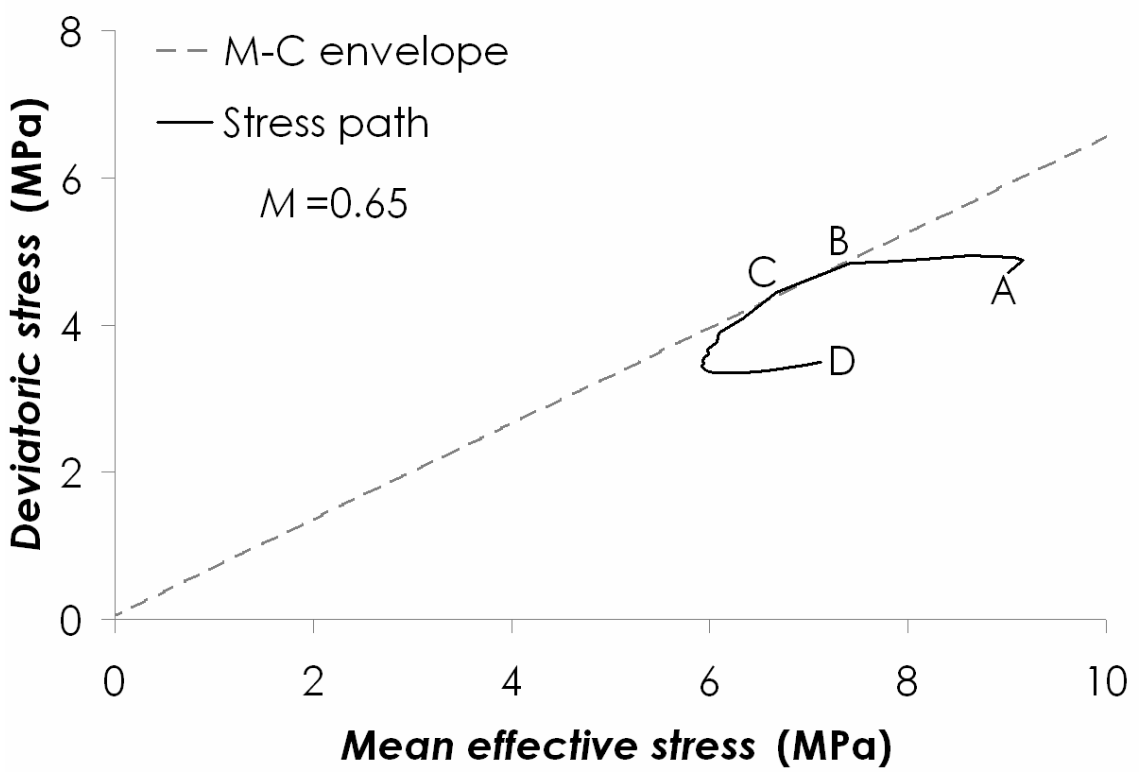

Figure 9: (*q, p'*) trajectory for a 100 day injection. The initial and final states are represented by A and D, respectively. The onset of plasticity takes place during early times (B-C), but plastic behavior eventually stops.

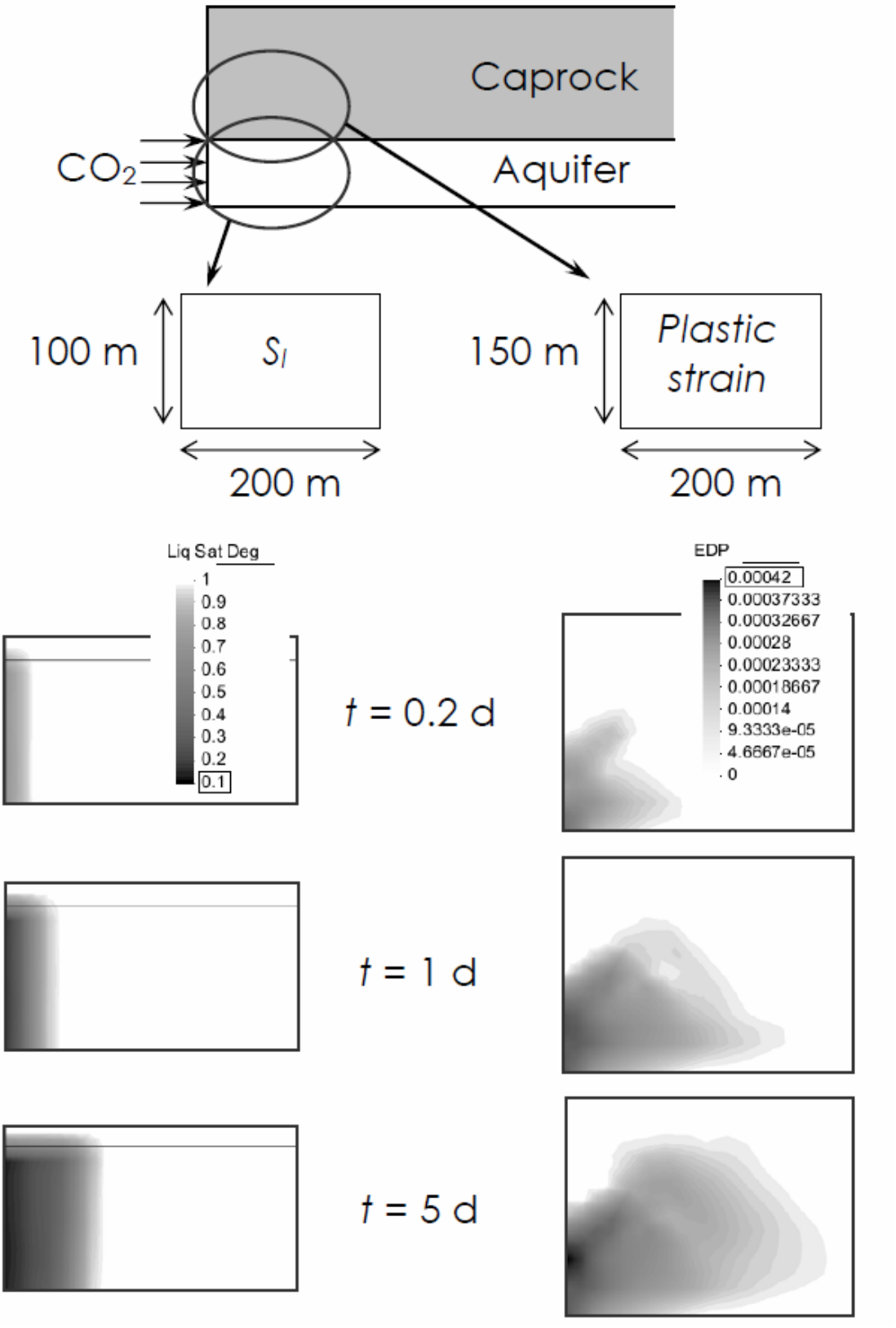

Figure 10: Plastic strain (*EDP*) in the caprock (left) and liquid saturation degree, S_l, in the aquifer (right) for different injection times. Plastic strain propagates as CO_2 advances at the beginning of injection.

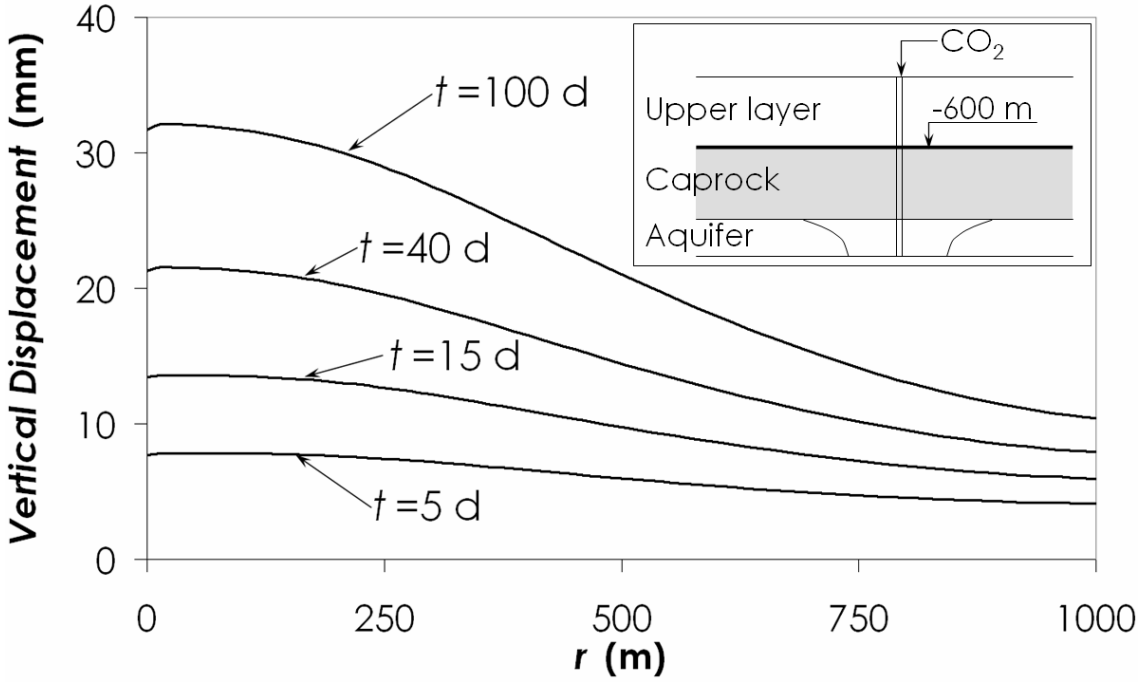

Figure 11: Vertical displacement as a function of distance from the well for different injection times at the top of the caprock (z = -600 m).